Energy & Environmental Science

Isothermally Crystallize Perovskites at Room-Temperature

Journal:	*Energy & Environmental Science*
Manuscript ID	EE-COM-06-2020-001967.R3
Article Type:	Communication
Date Submitted by the Author:	17-Aug-2020
Complete List of Authors:	Wang, Kai; Penn State University Park, Center for Energy Harvesting Materials and System; Virginia Tech Wu, Congcong ; Pennsylvania State University, Materials Science and Engineering Hou, Yuchen; Pennsylvania State University, Materials Science and Engineering Yang, Dong; Pennsylvania State University, Materials Science and Engineering Ye, Tao; Pennsylvania State University, Materials Science and Engineering Yoon, Jungjin; Seoul National University Sanghadasa, Mohan; U.S. Army, Aviation and Missile Research, Development, and Engineering Center, Weapons Development and Integration Directorate Priya, Shashank; Pennsylvania State University

Isothermally Crystallize Perovskites at Room-Temperature

Kai Wang,[1,2*] Congcong Wu,[3] Yuchen Hou,[1] Dong Yang,[1,2] Tao Ye,[1,2*] Jungjin Yoon,[1,2] Mohan Sanghadasa,[4] Shashank Priya[1,2*]

[1] Department of Materials Science and Engineering, Pennsylvania State University, University Park, PA 16802, United States
[2] Materials Research Institute, Pennsylvania State University, University Park, PA 16802, United States
[3] Hubei Collaborative Innovation Center for Advanced Organic Chemical Materials, Key Laboratory for the Green Preparation and Application of Functional Materials, Hubei Key Laboratory of Polymer Materials, School of Materials Science and Engineering, Hubei University, Wuhan 430062, China
[4] U.S. Army Combat Capabilities Development Command Aviation & Missile Center, Redstone Arsenal, Alabama 35898, United States

Abstract

Solution processability of photoactive halide perovskites differentiates them from traditional inorganic semiconducting materials that require multiple post-processing steps such as thermal/vacuum/blow- & solvent-assistant treatment. Here we report a technical breakthrough of isothermally crystallizing high-quality perovskite films at room-temperature (RT) without the necessity of any post-processing. This process takes advantage of our discovery of a metastable intermediate of lower-dimensionality formed by amine-assisted crystallographic lattice expansion from initial three-dimensional perovskite. Using *in-situ* optoelectrical/chemical and *ex-situ* structural characterizations, a detailed understanding of the low-dimensional metastable intermediate is developed. In conjunction with the metastable intermediate, the rapid evaporation of solvent and amine facilitates ultra-fast crystallization at RT within seconds. This RT rapidly synthesized perovskite film exhibits carrier diffusion length of 2.9 μm and {00ℓ} preferred orientation with an ultrahigh Lotgering factor of 97%. These films are highly compatible to conventional or inverted devices, demonstrating 22.3% and 23.1% power conversion efficiencies, respectively.

*Correspondence: K.W. (kaiwang@psu.edu); TY. (tvy5161@psu.edu); S.P. (sup103@psu.edu)

Introduction

Organic-inorganic halide perovskites (HPs) exhibit benign electronic band structure,[1] heavy-metal spin-orbital coupling,[2] polaronic charge transfer and electron-phonon coherence.[3,4] These characteristics impart attractive optoelectronic features such as large light-extinction, long carrier lifetimes and high charge carrier mobilities,[1,5] making them excellent candidates for photovoltaic (PV) applications. HPs can be easily processed using regular solution-processing techniques, such as spin-coating, which distinguishes them from traditional photovoltaic (PV) semiconductors such as silicon (Si), cadmium telluride (CdTe), copper indium gallium selenide (GIGS), etc.[6] There is continuous need to obtain PVs with low levelized-cost-of-electricity (LCOE) and simplified environment-friendly manufacturing techniques.[7] Here we demonstrate a fundamental breakthrough in manufacturing of HPs allowing the room-temperature (RT) isothermal crystallization within ten seconds.

Perovskite precursor inks typically consist of high-boiling-point solvents such as dimethylformamide (DMF), dimethyl sulfoxide (DMSO) and γ-butyrolactone (GBL) that require redundant solvent-removing steps (with elevated temperature of 70-150 °C) and long processing time (long-time solvent/thermal annealing and/or light sintering for facilitating Ostwald ripening)[8] to thermodynamically favor the crystal growth. Perovskite crystallization requires a chemical potential difference in order to drive the precipitation of crystals from precursor solution, which is proportional to the logarithm of supersaturation ratio.[9] The initiation of supersaturation can be achieved through temperature control (cooling),[10] concentration modulation,[11] or adjustments of the solution activity coefficients as those in the solvent/antisolvent methodologies.[12] Prior attempts on developing low-temperature synthesis process for HPs suffer from the use of nonvolatile ionic precursor system for initiating the supersaturation, and general RT processing is accompanied by subsequent laminar gas-blowing,[13] anti-solvent washing[14] or instant laser annealing.[15] In addition, all the prior processes require mild thermal annealing (TA) procedure in order to induce supersaturation to drive the crystallization (summarized and discussed in **Supplementary Note S1**). After crystallization, the residual high-boiling-point solvent molecules remaining within the polycrystalline film are believed to induce localized lattice distortion by forming perovskite-solvent chelated intermediates.[16] These residual chemicals within films introduce non-perovskite phases of poor electronic properties and severe scattering and recombination loss of photoexcited charge carriers. More volatile solvents such as 2-methoxyethanol (with a boiling point of

125 °C)[13,17,18] and other nonionic solvent systems[19] have been attempted which exhibit rapid drying behavior at RT and reduced ionic coordination with perovskite precursors. However, a TA process is inevitable in order to foster crystallization and remove remaining solvents.

Here we demonstrate a fundamentally transformative manufacturing strategy that enables rapid crystallization in ten seconds at RT without the need of any TA or postprocessing. This strategy takes advantages of an alcohol-soluble metastable intermediate formed by insertion of amine (R-NH_2) molecules into the perovskite crystallographic lattice. The fast solvent evaporation and spontaneous escape of amine from lattice induces a quick transition into the tetragonal β-phase perovskite crystals at RT. This approach leads to a high-quality polycrystalline thin film with ultrahigh [00ℓ] preferred orientation, ~2.8 μm charge diffusion length and super film uniformity. Solar cells designed using these ultra-fast synthesized perovskite films exhibit high power conversion efficiencies (PCEs > 22%) in both conventional and inverted configurations.

Results and discussion

Fig. 1A provides the evidence of effectiveness of this synthesis process. Text is written on paper by using this rapidly crystallizing perovskite ink at RT and this text is crystallized within seconds. This writing could be accomplished even at high relative humidity (RH) of ~90% (**Supplementary Video 1 (SV 1 Writing Crystal on Paper)**). We use various amine (R-NH_2) molecules coupled with different volatile solvents for preparing the ink and find a wide range of compatibility for the ink system. The options include methylamine, ethylamine and propylamine with solvent of ethanol, isopropanol and tetrahydrofuran (**fig. S1**). Unless otherwise stated, a prototype RT-ink containing $MAPb(I_{1-x}Cl_x)_3$ in mixed solvent system consisting of CH_3NH_2, EtOH, and acetonitrile is used here for the film and device fabrication and characterization in the following text. Both doctor-blade-coating and spin-coating processes (**Supplementary Video 2 (SV 2 Spin & Blade Coating)**) have been attempted and the film fabrication is found to be complete within 30 seconds (**Fig. 1B**). The crystallization mechanism has been studied in detail using *in-situ* optical microscopic study (in **Supplementary Note S2**). The RT isothermal crystallization follows the classic nucleation and crystal growth theory and we used the Avrami equation developed for the isothermal conditions to reveal the kinetic nature of the crystallization. An Avrami constant (n)[20] has been obtained with a value of n = 3.63 > 3, suggesting that the crystal growth involves a three-dimensional growth with a rapid nucleation due to the fast supersaturation. Scanning electron microscopy (SEM)

analysis shows that the RT isothermally crystallized perovskites (RT-perovskite) exhibit film morphology consisting of densely packed hexagonal grains with an average size of *ca.* 700 nm (**Fig. 1C**). In the out-of-plane direction, there is only single large grain (**fig. S2A**) throughout the film (**Fig. 1D**), suggesting a well-aligned crystal growth during the RT isothermal process. To further prove this, we also compare the SEM images of the perovskite film prepared from the typical ink followed by a thermal-annealing process (TA-perovskite) (**fig. S2B**). The top-view SEM image of TA-perovskite displays various grain boundaries and a nonuniform surface meanwhile the cross-sectional images exhibits a less aligned grain feature, consistent to its X-ray diffraction (XRD) result (**fig. S2B**), indicating the co-existence of multiple scattering facets in the vertical direction. In comparison, the RT-perovskite exhibits well aligned grains (**Fig. 1D & fig. S2B(iii)**). We also estimate the trap density of different films in **fig. S2B(iv)** by a space charge limited current (SCLC) method and observe a four-fold lower trap density of RT-perovskite (1.6×10^{15} cm^{-3}) than the TA-perovskite (6.5×10^{15} cm^{-3}). These vertically aligned single grains in the RT-perovskite secure the efficient out-of-plane flow of charge carriers in two-terminal PV cells, as the photogenerated carriers only transport within one single perovskite grain to reach corresponding electrodes and do not encounter grain boundary. Such transit avoidance of grain boundary minimizes the scattering loss by disorder states[21] and reduces the recombination loss by ionic impurities or traps (Shockley-Read-Hall recombination) located at grain-boundaries.[22] At a larger scope of 10-100 μm, the RT-perovskite film displays an ultrahigh uniformity as viewed from the cross-sectional SEM (**fig. S3**) and a specular surface in a macroscopic view (**fig. S1B**). We also tune the composition of the perovskite system of $MAPb(I_{1-x}Cl_x)_3$. By changing x from 0 to 0.1 (**fig. S4**), we obtained an optimal crystal-grain feature at $x = 0.05$. Hence, a perovskite of $MAPb(I_{1-x}Cl_x)_3$ with a $x = 0.05$, is used for the following investigation. In order to distinguish this ink that could isothermally crystallize at room-temperature (RT-ink) from those typical inks that need a thermal annealing process (TA-ink). We tested the ionic current through a cyclic voltammetry measurement using both inks as electrolyte. The TA-ink shows an ionic current over 200 μA under 0.4 V (**Fig. 1F**), which is over three-order-magnitude larger than that of 100 nA from the RT-ink (**Fig. 1E**). This indicates a significantly lower concentration of ions in the RT-ink. In addition, we also execute an electrolytic cell test. Both inks are supplied by a 1.5 V DC bias for 5 hr. As can be seen in the photography inserted in **Fig. 1F**, the color of the TA-ink turns into orange due to the precipitation of I_2. And at the cathode, there are precipitation of lead. This result

verifies the existence of free I^- and Pb^{2+} in the original TA-ink which can experience a redox reaction under external bias. In contrast, the RT-ink does not show such observation (**Fig. 1E**), suggesting the formation of already assembled intermediate clusters so that there is minimized free ions in the system.

To further understand the compositional evolution during the RT isothermal crystallization process, we employed an *in-situ* steady-state photoluminescence (PL) study (**fig. S9**). During the drying of the wet film, there is a notable redshift of the PL peak (**Fig. 2B**), indicating a bandgap reduction as schematically depicted in **Fig. 2A**. As the electronic band structure in momentum space is correlated with the crystallographic structure in real space,[23] this PL change is an indication of the crystallographic phase evolution from some metastable intermediate states to the final tetragonal β-phase states during the RT isothermal crystallization. Based upon the PL emission wavelength, we classify this RT isothermal process into three states (**Fig. 2B**): (i) wet film (from 0 to 40 s, no obvious PL emission), (ii) drying intermediate (from 40 to 207 s, PL gradually red-shifts towards 806 nm) and (iii) dry perovskite (after 207 s, PL peak fixed at 806 nm). Samples of a drying intermediate and a final dry perovskite films were analyzed to compare their individual PL feature in the excitation-emission map (**Fig. 2C**). By exciting with an identical light source with a wavelength range from 300 to 350 nm, the dry perovskite displays a narrow emission peak at 806 nm. In contrast, the intermediate phase shows a wide emission range peak at a short wavelength around 750 nm, indicating a gradual metamorphosis with larger bandgap. To understand this larger bandgap intermediate phase, we characterize both the chemical and structural fingerprint. A thermogravimetric analysis (TGA) coupled with an *in-situ* mass spectroscopy (MS) technique is employed to trace the whole RT isothermal crystallization process. **Fig. 2D** shows the TGA and temperature curve, including three thermal steps of RT-isothermal drying (before 1820 s), warming to 100 °C (1820 to 2270 s) and 100 °C isothermal treatment (after 2270 s). During the RT isothermal step, there is a spontaneous weight loss which results from the evaporation of solvents (ACN and EtOH) and the amine (MA, or methylamine), as characterized by the *in-situ* MS in **Fig. 2E**. After 1200 s in the RT isothermal process, the weight loss reaches to a saturation as all the volatile molecules have evaporated. The weight remains constant even after warming up to 100 °C and holding there. This indicates that all the volatile molecules have already evaporated during the RT isothermal drying process. Overall, the final weight ratio remains

constant at 57.5 wt.%, which agrees well with the starting concentration of the ink. Such RT isothermal crystallization is quite different from that of conventional TA-perovskite.

We compare the TGA-MS spectra of whole crystallization process of RT- and TA-perovskite in **fig. S12** and find that in TA-perovskite the solvent evaporation of DMF only occurs at elevated temperatures and needs over 40 minutes for removal due to the much higher boiling point of DMF (153°C). In comparison, the RT-perovskite ink displays a rapid co-evaporation of solvent molecules and amine, leading to the quick phase transition from the intermediate state to the final perovskite crystal. This intermediate phase exhibits larger bandgap and shows a quick transition to the tetragonal β-phase perovskite at RT. To further characterize the intermediate state, we modify the synthesis of the RT-ink by dispersing the perovskite single crystal in a highly concentrated amine solution at lower temperature and obtain the intermediate state in a form of single crystal (**fig. S13**). The intermediate perovskite displays a colorless feature with a large optical bandgap of 2.26 eV (**fig. S14**), which corresponds to the increased $\{00\ell\}$ interplanar distance[1] in the crystallographic lattice according to the X-ray diffraction (XRD) analysis presented in **Supplementary Note S3**. This increase of interplanar $\{00\ell\}$ spacing can be ascribed to the insertion of amine molecules between the neighboring $[PbI_6]^{4-}$-octahedral sheets, bridging by hydrogen-bond interactions[24,25] and formation of the lower-dimensional metastable intermediate of $MA(A)_nPb(I_{1-x}Cl_x)_3$, where A is amine and we use I, and Cl as mixed halogen as it exhibits higher charge carrier mobility.[26] The intermediate state contains the coordination of Pb with both halogen and amine (**fig. S15**). During the RT isothermal process, amine molecules escape (driven by the high tendency of evaporation due to the low boiling point, bp, of amine, e.g., -6°C of MA) from the lattice leading to the interplanar distance reduction as schematically depicted in **Fig. 2F**. This spontaneous process at RT leads to the lattice collapse from the intermediate lamellar structure to the final tetragonal β-phase. To quantify, **Fig. 2G** shows the XRD result. The intermediate perovskite displays a $\{00\ell\}$ interplanar distance of 12.33 Å corresponding to a (002) XRD peak at 7.16°, while in distinct contrast the final tetragonal β-phase perovskite displays an interplanar distance of 6.32 Å corresponding to a (002) peak at 14.01°. Hence during the RT isothermal process, the trapped amine molecules within the perovskite intermediate could escape the lattice along with the evaporation of volatile solvents which leads to the lattice size reduction from a lower-dimensional planar structure with a larger *c*-axis interplanar distance to a three-dimensional structure with a *c*-axis shrunken lattice. This structural evaluation gives rise to the PL

peak redshift in **Fig. 2B**. Interestingly, we find the intermediate film exhibits a strong orientation along the [00ℓ] direction, which has been successfully inherited to the final tetragonal β-phase. Accordingly, the resultant RT-perovskite film exhibits a strong [00ℓ] orientation (**fig. S16**) with an ultrahigh Lotgering factor[27] of 97%. This highly ordered lattice packing is expected to generate reduced disordered electronic states and induce a higher charge transport property.

We then utilize the optoelectronic study to characterize the electrical transport property of the RT-perovskite. Tauc plot (in accordance of direct transitions) reveals an optical bandgap of 1.55 eV and the time-integrated PL displays a narrow full width at half maximum (FWHM) of 72 meV (**fig. S17**), close to that of single crystals.[28] Prior reports have shown a range of bandgap from 1.55 eV to 1.6 eV for the TA-perovskites of the identical composition,[29,30] while here we found the RT-perovskite displays a consistent bandgap of 1.55 eV regardless of either powder or crystal precursors (**fig. S17C**). This suggests the RT isothermal crystallization methods is more reliable in reproducing high quality crystals, as the crystalline fingerprint such as degree of crystallinity, orientation and grain structure have a strong influence on their optical and electronic properties and a highly controllable crystalline feature in RT perovskite leads to a consistent bandgap. The electronic properties (such as the charge carrier diffusion length defined as the average distance that an excited carrier will travel before recombining) are important in determining the overall performance of optoelectronics. Longer diffusion lengths are indicative of efficient transport and better device performance, which could also be originated from a higher crystal quality. The carrier diffusion length is measured through the PL spectroscopy on perovskite in presence or absence of a quenching layer. SnO_2 and Spiro-OMeTAD have been used as electron and hole quencher respectively due to their picosecond charge extraction ability when interfacing with perovskite.[31,32] By comparing time-resolved and time-integrated PL on bare perovskite against perovskite/SnO_2 and perovskite/Spiro-OMeTAD, carrier diffusion signatures of different perovskites can be achieved. For RT-perovskite, the time-integrated PL shows significant quenching after interfacing with either SnO_2 or Spiro-OMeTAD (**fig. S18** shows a quenching factor of 24 and 40 upon SnO_2 and Spiro-OMeTAD, respectively). These high-degree quenching comparable to that in donor-acceptor bulk heterojunction (BHJ) systems[33] suggests sufficient charge extraction. Time-resolved PL reveals substantially shortened lifetimes of 18.1 and 16.9 ns upon interfacing with SnO_2 and Spiro-OMeTAD, respectively, in distinct contrast to the bare perovskite of 5.3 μs (**Fig. 3A**). Similar trends are found in the reference film of TA-perovskite in **Fig. 3B**. Notably, RT-perovskite

exhibit a much longer carrier lifetime of 5.3 μs than that of 310.2 ns in TA-perovskite. This could be ascribed to the higher crystalline quality of the RT-perovskite film and indicates reduced scattering loss. Overall, both perovskites exhibit sufficiently quenched PL yield and mono-exponentially decayed lifetime with significantly shortened number upon interfacing quenching layers. These results are compared with the carrier diffusion length obtained by the following equation derived from Continuum theory using a diffusion model (detailed in **Supplementary Note S4**):[34]

$$\frac{L_D}{L} = \frac{2}{\pi}\sqrt{\frac{1}{\tau_D/\tau_0} - 1} \qquad (1)$$

with L_D being the diffusion length, L the film thickness, τ_D and τ_0 the monoexponentially fitted lifetimes in presence or absence of quencher, respectively. **Fig. 3C** displays the plot of L_D against τ_D/τ_0 where the diffusion length of 2.9 and 2.8 μm of hole and electron respectively are found in RT-MAPb$(I_{1-x}Cl_x)_3$ perovskite film with 3-fold larger than those of 917 and 883 nm in TA-MAPb$(I_{1-x}Cl_x)_3$ perovskite. The μm-scale diffusion length in these Cl-doped I-based TA-perovskite[35] is ascribed to the halogen ionic-radii difference that stabilizes the phase of the continuous solid solution,[29] or slower MA rotational dynamics evidenced in quasielastic neutron scattering (QENS) investigations[36] or other mechanisms.[37] Higher crystallinity leads to more efficient charge transport and in the limited case of single-crystalline MAPb$(I_{1-x}Cl_x)_3$, the diffusion length exceeds 380 μm.[38] The RT-perovskites display long diffusion length on the order of 2.8~2.9 μm, which can be related to the highly ordered crystalline packing and [00ℓ] orientation inherited from the intermediate state during the RT isothermal crystallization. The balanced electron and hole diffusion also imply a balanced charge transfer in device.

To evaluate the photovoltaic performance of solar cells based on these RT-perovskites and qualify their performance in devices, we prepared both conventional (p-i-n) and inverted (n-i-p) structured PVs. The conventional device consists of fluorine-doped tin oxide (FTO)/compact-TiO_x (c-TiO_x, considering the oxygen vacancy,[39,40] a substoichiometric expression of "TiO_x" rather than the "TiO_2" is used here)/mesoporous-TiO_x (m-TiO_x)/RT-perovskite/Spiro-OMeTAD/gold (Au), with FTO being the front cathode collecting electrons and Au being the back anode collecting holes respectively. **Fig. 3D** shows a cross-sectional SEM image of the conventional device, visualizing the layer-by-layer device structure. The RT-perovskite layer displays a uniform thickness of *ca.* 420 nm and an ultra-flat surface, even when viewed over a larger surface area (**fig.**

S19). This enables a homogeneous electrical contact with top buffer and back electrode. Under AM 1.5 illumination, the RT-perovskite based conventional device exhibits a PCE of 22.32% (independently certified at 22.28% in **fig. S20**) with a short-circuit current (J_{SC}) of 24.33 mA cm^{-2}, open-circuit voltage (V_{OC}) of 1.16 V and fill factor (FF) of 79.1% under reverse scan condition (from positive bias to zero), and 24.35 mA cm^{-2}, 1.154 V, and 78.32% with a PCE of 22.01% under forward scan condition (from zero to positive bias) (**Fig. 3E (i)**). In comparison, the TA-perovskite device exhibits a relatively lower PCE of 20.03% under reverse scan condition and even lower PCE of 19.01% under forward scan condition. Incident photon-to-electron conversion efficiency (IPCE) spectroscopy coupled with photocurrent integration reveals an integrated current of 24.24 and 23.67 mA cm^{-2} for RT- and TA-perovskite based device respectively (**fig. S21**), in good agreement with numbers (24.33 and 23.91 mA cm^{-2} respectively) extracted from photocurrent density-voltage (J-V) characteristics. Notably, the RT-perovskite device displays a noticeable increase in FF, with a higher shunt resistance (R_{sh}) of 4.9 kΩ cm^2 and smaller series resistance (R_s) of 3.8 Ω cm^2, respectively, compared to that of R_{sh}= 0.93 kΩ cm^2 and R_s= 5.7 Ω cm^2 from TA-perovskite based device. This is consistent with the long carrier diffusion length of RT-perovskite and is indicative of efficient charge transport behavior throughout the device. Particularly at the perovskite/spiro-OMeTAD interface, the flat surface of perovskite secures a synchronized charge transfer from the perovskite to the spiro-OMeTAD buffer in terms of the whole interface thereby less higher order carrier recombination. **Fig. 3E (ii)** compares the static photocurrent of devices biased at their corresponding maximum power points (V_{mp}). The V_{mp} for each device is individually calculated from **fig. S22**. The RT-perovskite device displays a stabilized maximal output power of 22.36 mW cm^{-2} corresponding to a PCE of 22.36% consistent with the number of 22.32% obtained from J-V characteristics. In comparison, the TA-perovskite exhibits a mild value of 19.88 mW cm^{-2} (corresponding to a PCE of 19.88%), which is consistent with the typical state-of-the-art values.[41] We also investigate the statistics of conventional device using either RT- or TA-perovskite in **Fig. 3F** by measuring photovoltaic parameters from 20 individual device. The data for the RT-perovskite based devices exhibit a narrower distribution, as indicated by a smaller standard deviation (σ) shown in **Table S4** ($\sigma_{RT,\,PCE}$= 0.48% vs. $\sigma_{TA,\,PCE}$= 0.82%).

Inverted solar cells consisting of indium tin oxide (ITO)/NiO_x/RT-perovskite/phenyl-C_{61}-butyric acid methyl ester (PCBM)/bathocuproine (BCP)/silver (Ag) have been prepared and

characterized to further evaluate the performance of RT-perovskite. **Fig. 3G** displays the cross-sectional SEM images of the fabricated devices. Similar to the conventional device, the inverted structure with RT-perovskite thin film coated on top of NiO_x also exhibits excellent uniformity and ultrahigh flatness as seen in **fig. S23**. This homogeneity is important for the efficient charge transfer across the backside contact from microscale and correlates to a higher performance at device scale, as leakage, shunting and other meso-structural defects are minimized due to the high film uniformity. Accordingly, the crystallinity, homogeneity and charge transport property of the RT-perovskite enables a high PCE of 23.07% in the inverted device, coupled by simultaneously improved J_{SC} of 23.52 mA cm^{-2}, V_{OC} of 1.158 V and FF of 84.70% under a reverse scan condition (from positive bias to zero), and 24.48 mA cm^{-2}, 1.156 V and 84.58% with a PCE of 22.96% under a forward scan condition (from zero to positive bias) (**Fig. 3H (i)**). In comparison, the TA-perovskite devices exhibit substantially lower PCE of 20.85% (under reverse scan) and 19.88% (under forward scan). We notice a significant improvement in FF from 78.9% to 84.7% owing to the superior charge transport property of the RT-$MAPb(I_{1-x}Cl_x)_3$ perovskite and an obvious voltage change from 1.142 to 1.158 V. Such a change is also present in conventional structured devices (**Fig. 3E (i)**).

In solar cells V_{OC} is determined by the quasi-Fermi level (quasi-FL) separation at the contacts and in ideal case it corresponds to the quasi-FL separation in the absorber, assuming infinite carrier mobility and well-aligned bands. In practice, the finite electron and hole conductivities limit the carrier transport by a potential loss, which is reflected in the quasi-FL gradients and finally an internal voltage drop. More efficient charge transport corresponds to lower charge losses (multiple recombination mechanisms including Shockley-Read-Hall recombination and higher order nongeminate recombination etc.)[42] and less potential losses within the device and hence simultaneously enlarged FF and V_{OC}. Another result of efficient charge transfer is a higher external quantum efficiency of photon to current conversion. The corresponding IPCE spectra also verifies a higher quantum efficiency in the RT-perovskite device, showing an integrated current density of 23.22 mA cm^{-2}, which is larger than that of 22.78 mA cm^{-2} in TA-perovskite device (**fig. S24**). **Fig. 3H (ii)** compares the static efficiency of the inverted devices biased at their own corresponding V_{mp} extracted from power-bias curve in **fig. S25**. The RT-perovskite device shows a steady maximal output power of 23.06 mW cm^{-2}, corresponding to a PCE of 23.06% higher than the TA-counterparts of 20.55 mW cm^{-2} and a higher consistency with

the PCE values obtained from J-V characteristics. We also compare the statistics of inverted devices using the data obtained from 20 individual devices. As shown in **Fig. 3I**, the solar cells fabricated using RT-perovskite exhibit higher average parameters and a narrower distribution compared to their TA-counterparts. Specifically, the RT-perovskite device displays a PCE of 22.10 ± 0.49% (mean ± standard deviation) compared to that of 20.29 ± 0.93% from TA-perovskite device. The smaller standard deviation (σ) implies a higher reproducibility ascribed to the excellent film uniformity and high surface flatness.

Conclusion

In addition to the $MAPb(I_{1-x}Cl_x)_3$ RT-perovskite, we also synthesize the RT-perovskite with compositions of $MAPbI_3$ and $MAPb(I_{1-x}Br_x)_3$ and characterize the corresponding device performance. Both perovskites exhibit fast crystallization isothermally at RT with a specular film surface. The corresponding device also shows an enhanced efficiency: RT-$MAPbI_3$ based device shows a PCE of 21.93% compared to that of 19.50% from its TA-counterpart (**fig. S26**); RT-$MAPb(I_{1-x}Br_x)_3$ based devices show a PCE of 22.19% compared to that of 20.06% from its TA-counterpart (**fig. S27**). These results clearly demonstrate the effectiveness and high performance of the isothermally crystallized RT perovskite ink for fabrication of efficient solar cells. We attribute this exciting achievement to the volatile solvent and metastable intermediate state that synergistically foster a rapid phase transition at RT. Overall, we have developed the proto RT-ink (with a CH_3NH_2/EtOH/Acetonitrile solvent system) for isothermally crystalize the perovskite which sets an over 22% efficiency baseline for RT-perovskite solar cell. Using this RT-ink protocol, by further exploring other amine and volatile solvent candidate (as exemplified in **fig. S1**), delicately tuning the compositions and their ratios, and expanding their universality to more other perovskites, we anticipate there will be more opportunities in the future that could be deviated from this paradigm methodology.

Methods

Materials. Lead (II) bromide ($PbBr_2$, 99.99%), Lead (II) iodide (PbI_2, 99.99%) and Lead (II) iodide (PbI_2, 99.99%) were purchased from Alfa Aesar. Spiro-OMeTAD, TiO_2 paste (18NR-T), FTO/glass (ITO/glass) were purchased from Luminescence Technology Corp, Dyesol, and Nippon Sheet Glass, respectively. Other chemicals were purchased from Sigma-Aldrich and used without further purification. These chemicals include: methylammonium iodide (MAI), methylammonium bromide (MABr), methylammonium chloride (MACl), amine solutions including ammonia

solution (28-30 wt.% in water and 2.0 M in ethanol), methylamine solution (33 wt.% in absolute ethanol, 40 wt.% in water and 2.0 M in tetrahydrofuran), ethylamine solution (2.0 M in tetrahydrofuran) and propylamine (≥99%) and solvents such as dimethylformanmide (DMF, extra dry, 99%), dimethyl sulfoxide (DMSO, extra dry, 99%), 1, 2-dichlorobenzene (DCB, extra dry, >98%), chlorobenzene (CB, extra dry, 99.8%), and isopropanol (extra dry, 99.8%).

Single-crystal synthesis. Single-crystals of $MAPbI_3$, $MAPb(I_{1-x}Cl_x)_3$ and $MAPb(I_{1-x}Br_x)_3$ were synthesized according to prior reports.[43] Taking $MAPbI_3$ as an example, a precursor solution containing 5.54 g PbI_2 and 1.91g MAI in 10 mL GBL was prepared at 70 °C, followed by filtration with a PVDF filter with pore size of 0.2 μm. The resultant pale-yellow solution was transferred into an oil bath with a gradual temperature increase from RT to 110°C within 2 hrs. and maintained at 110 °C for 3 hrs. After that, single crystals of black $MAPbI_3$ perovskite were obtained, which were further cleaned by diethyl ether washing and then dried in a vacuum oven overnight. For $MAPb(I_{1-x}Cl_x)_3$ and $MAPb(I_{1-x}Br_x)_3$ perovskite, small amount (3 mol% to 5 mol%) of PbX_2 and MAX (X is either Cl or Br) were added to above PbI_2 and MAI precursors and 2.5 vol% DMSO was added as an secondary solvent.[44] Other steps are similar to that for $MAPbI_3$.

Room-temperature isothermally crystallized perovskite ink (RT-ink) preparation. The RT isothermally crystallized perovskite ink was prepared by dispersing above single crystals into a series of amine-solutions, where the amine could be ammonia (NH_2), methylamine (CH_3NH_2) and propylamine ($CH_3(CH_2)_2NH_2$), etc., and solvent could be water, ethanol, isopropanol, tetrahydrofuran, etc. (as can be seen in **fig. S1**). Additionally, solvent of acetonitrile was further added into above system to dilute the solution towards a final concentration of 1.0 to 1.2 M. For example, in the case of the $MAPb(I_{1-x}Cl_x)_3$ RT-ink (using CH_3NH_2/EtOH) used in the solar cell preparation, 734 mg $MAPb(I_{1-x}Cl_x)_3$ single crystal was added in 600 μL CH_3NH_2/EtOH (33 wt.%) and further diluted by 400 μL acetonitrile to synthesize a 1.2 M ink. For other RT-inks shown in **fig. S1**, all are prepared by dispersing perovskite crystals into a mixture solution of (1) amine (could be NH_2, CH_3NH_2 and $CH_3(CH_2)_2NH_2$), etc.), (2) a volatile solvent (could be water, ethanol, isopropanol, tetrahydrofuran, etc.), and (3) acetonitrile. The final concentration of perovskite and amine is 1.2 M and 4.8 M, respectively. The volume ratio between volatile solvent and acetonitrile is 6:4. After ultrasonication (110 W, 40 kHz) for 10 minutes, yellowish solution was obtained, which will be used for RT isothermal crystallization later. It should be noted that all the amines and solvents for this system have low boiling point. The whole ink preparation was executed at room temperature in an ambient atmosphere. The ink was used after preparation and normally a storage in refrigerator less than 48 hrs. would not significantly affect the result. But a direct use after preparation and an ultrasonication before use are suggested.

Spin-coating room-temperature isothermally crystallized perovskite (RT-perovskite) thin film. The RT-perovskite thin film was spin-casted from above RT-ink with a spin-rate of 4,000 to 6,000 r.p.m. for 60 s through a dynamic spin-coating process. Here the dynamic spin-coating

process refers to a process where the ink is dropped on an already steadily spinning substrate. As shown in **Supplementary Video (SV 2. Spin & blade Coating)**, the film exhibited a quick color change into a black film within several seconds. A relative long spinning period of 60s was used to adequately remove the solvent. We used this spin-coating method to prepare the RT-perovskite film for solar cells.

Doctor-blading RT-perovskite thin film. The RT-ink also exhibited good compatibility for RT-processed blade coating. **Supplementary Video (SV 2. Spin & blade Coating)** also shows a primitive blade coating process on a glass substrate using above RT-ink. In this preliminary blade process, we used a glass rod to spread the ink on a UV-plasma treated FTO/glass substrate. The RT-ink displayed good wettability on the substrate and the wet film also exhibited a quick darkening upon solvent evaporation within several seconds.

Solar cell fabrication. *Conventional (n-i-p) structure:* The n-i-p device with an architecture of FTO/c-TiO_x/m-TiO_x/RT-perovskite/Spiro-OMeTAD/Au was used to evaluate the photovoltaic performance of the RT-perovskite. The FTO/glass substrates were first ultrasonicated in bath of detergent, deionized water, acetone and isopropanol successively, followed by drying in an oven overnight. After that, the dried substrate was further cleaned by UV ozone plasma for 45 min. A compact layer of TiO_x was then spin-coated on these precleaned FTO/glass substrates from a mildly acidic titanium isopropoxide solution (prepared by slowly adding mixed solution containing 35 μL 2M HCl and 2.53 mL ethanol into another mixed solution of 369 μL titanium isopropoxide and 2.53 mL ethanol) with a spin-rate of 2,000 r.p.m., followed by thermal annealing at 150 °C for 10 min. A mesoporous TiO_x layer was then spin-coated on top of the compact layer at a spin-rate of 6,000 r.p.m., from an ethanol solution containing TiO_2 paste (18NR-T), α-terpineol and ethanol (TiO_2: α-terpineol: ethanol = 1:3:1.5 wt%). After that, the substrate coated with both TiO_x layers were annealed at 500 °C for 1 hr. After cooling down to RT, the substrates were further treated by UV ozone plasma for 15 min. The RT-perovskite layers were then spin-coated on top according to above methods. Notably, the RT-perovskite experienced a quick phase transition and no additional processing (neither anti-solvent process nor post-solvent annealing) was needed. A Spiro-OMeTAD layer was then spin-casted on top with a spin-rate of 4,000 r.p.m. Finally, a 75 nm gold electrode was thermally deposited to finalize the device.
Inverted (p-i-n) structure: The p-i-n device with an architecture of ITO/NiO_x/RT-perovskite/PCBM/BCP/Ag was used to evaluate the photovoltaic performance of the RT-perovskite. The pre-cleaned ITO/glass substrates (through ultrasonication in bath of detergent, deionized water, acetone and isopropanol sequentially) were treated by UV-ozone plasma for 40 minutes before use. A ~40 nm thick NiO_x was spin-casted from NiO_x nanocrystal solution at a spin-rate of 3000 rpm for 40 s according to prior reports.[45] The RT-perovskite photoactive layer was spin-coated on top of NiO_x according to above method using the RT-ink. After that, a PCBM electron transfer layer was spin-coated on top of perovskite using a PCBM/chlorobenzene solution (10 wt.%) at a spin-rate of 1000 r.p.m. for 50 s. Lastly, a 5 nm thick bathocuproine (BCP) and 100

nm thick aluminum (Al) film were sequentially deposited on top through a shadow mask in the vacuum of $<5\times10^{-6}$ mbar to finalize the device.

Material characterization. All the scanning electron microscope (SEM) images were obtained from a LEO 1530 MERLIN (FESEM) in the Nanofabrication lab in Material Research Institute (MRI) at Penn State. For perovskite material, the acceleration voltage was determined to be 5 kV. Both secondary electron (SE) and backscattered electron (BSE) detection through in-lens secondary electron detectors and conventional Everhart-Thornley style detectors respectively were used during the characterization. The atomic force microscopy (AFM) and conductive-AFM (C-AFM) images were recorded through a Bruker Innova AFM platform from the Energy and Environmental Sustainability Laboratories (EESL). The sample was coated directly on an ITO/glass substrate which was further contacted with the bottom electrode of the AFM platform. A Pt-coated AFM tip was used as the top moving electrode at a scan rate of 1.0 Hz. The *in-situ* isothermal RT crystallization study through an optical microscopy and corresponding video (**Supplementary Video [SV 4. In-situ OM Observation]**) was recorded on an OlympusMX50 microscopy in the Material Characterization Lab (MCL) at Penn State. TGA/MS study was performed on a Discovery Series TGA Q5500 coupled with Discovery MS (TA instruments). When coupled to MS, the gaseous species that were released as a result of evaporation were transferred to MS through heated capillary transfer line. The quadrupole detector in MS provides chemical determination (mass/charge from 1 to 300) of evolved gases giving information about reactions in real time. The *in-situ* PL study on the RT isothermal crystallization process was performed on the FLS1000 Photoluminescence Spectrometer (Edinburgh Instruments). Specifically, RT-ink was directly dropped on a glass substrate which was under a repeat scan by the Spectrometer. To acquire a high time resolution, data point for each single PL spectra was reduced to a number of 31. For the time-integrated PL map, samples were tested at various excitation (300 to 350 nm) and emission wavelengths (420 to 940 nm). The excitation incident takes place at the perovskite thin film surface with the opposite side being the quenching layers in cases of quenching experiment. For the charge carrier diffusion length study, the time-resolved PL of different samples were excited at 650 nm and detected at 800 nm. For each sample, same incident intensity and optical path was applied. The UV-vis absorption spectroscopy was measured by UH4150 (HITACHI). XRD patterns were obtained by a Malvern Panalytical Empryean X-Ray Diffractometer (Cu Kα radiation, Rietveld refinement of the PXRD data were performed with the General Structure Analysis System (GSAS) software).

Device characterization. All the solar cell devices were tested under one one-sun illumination (AM 1.5) provided by Xenon solar simulator (Solar Simulator, Class AAA, IEC/JIS/ASTM, 450 W Xenon, 2 × 2 in.) in the ambient atmosphere. The intensity of the simulator was calibrated to 100 mW cm^{-2} by using a standard reference Si solar cell (Calibrated Reference Cell, Meter, KG3 Window, certified by NREL). The spectral mismatch factor was maintained in a narrow range of 0.99 to 1. The device area (0.096 cm^2) was defined by a metal aperture placed on top of the cell.

J-V curves were obtained by either reverse (high voltage to low voltage) or forward scan (low voltage to high voltage) with a scan step of 20 mV and scan rate of 200 mV/s, if not state otherwise, using a Keithley digital source meter (Model 2,400). The static output power was measured by recording the continuous photocurrent of the device hold at a constant voltage bias close to its maximum power point (V_{mp}). The V_{mp} was determined by plotting the power against the voltage. The photocurrent tracking was performed by Electrochemical Workstations programmed in a current-time characterization. The IPCE was recorded by the QuantX 300 (ORIEL) in ambient atmosphere.

Author contributions

K.W. designed the research and S.P. supervised the whole project. K.W., C.W. and Y.H. synthesized the materials, fabricated the devices and characterized the device performance. K.W. and Y.H. performed other characterizations in MCL. D.Y., T.Y. and J.Y. helped in analyzing the data. K.W. wrote the manuscript and all the authors were actively involved in the discussion, analysis and revision.

Conflicts of interest

The authors declare no competing interests.

Acknowledgments

We are grateful to Material Characterization Lab (MCL) and Nanofabrication Lab in Penn State for assistance with material characterization tests. We also thank South China Academy of Advanced Optoelectronics for independent efficiency authentication tests. K.W. and Y.H. acknowledge the support from Air Force Office of Scientific Research under award number FA9550-17-1-0341. S.P. acknowledges the financial support from the Office of Naval Research through grant number N000141912461. D.Y. acknowledges the support from NSF-Crest grant number HRD 1547771. TY and JY acknowledge the support from Office of Naval Research through grant number N000141712520.

References

1 K. Wang, D. Yang, C. Wu, M. Sanghadasa and S. Priya, *Prog. Mater. Sci.*, 2019, **106**, 100580.

2 T. M. Brenner, D. A. Egger, L. Kronik, G. Hodes and D. Cahen, *Nat. Rev. Mater.*, 2016, 1, 1–16.

3 F. Thouin, D. A. Valverde-Chávez, C. Quarti, D. Cortecchia, I. Bargigia, D. Beljonne, A. Petrozza, C. Silva and A. R. Srimath Kandada, *Nat. Mater.*, 2019, **18**, 349–356.

4 A. D. Wright, C. Verdi, R. L. Milot, G. E. Eperon, M. A. Pérez-Osorio, H. J. Snaith, F. Giustino, M. B. Johnston and L. M. Herz, *Nat. Commun.*, 2016, **7**, 1–9.

5 L. M. Herz, *ACS Energy Lett.*, 2017, 2, 1539–1548.

6 A. Rajagopal, K. Yao and A. K. Y. Jen, *Adv. Mater.*, 2018, 30. 1800455.

7 T. Matsui, J.-Y. Seo, M. Saliba, S. M. Zakeeruddin and M. Grätzel, *Adv. Mater.*, 2017, **29**, 1606258.

8 Z. Li, T. R. Klein, D. H. Kim, M. Yang, J. J. Berry, M. F. A. M. Van Hest and K. Zhu, *Nat. Rev. Mater.*, 2018, 3, 1–20.

9 K. Wang, C. Wu, Y. Hou, D. Yang and S. Priya, *J. Mater. Chem. A*, 2019, **7**, 24661–24690.

10 V. L. Pool, B. Dou, D. G. Van Campen, T. R. Klein-Stockert, F. S. Barnes, S. E. Shaheen, M. I. Ahmad, M. F. A. M. Van Hest and M. F. Toney, *Nat. Commun.*, 2017, **8**, 1–8.

11 B. wook Park, N. Kedem, M. Kulbak, D. Y. Lee, W. S. Yang, N. J. Jeon, J. Seo, G. Kim, K. J. Kim, T. J. Shin, G. Hodes, D. Cahen and S. Il Seok, *Nat. Commun.*, 2018, **9**, 1–8.

12 C. Liu, Y. Cheng and Z. Ge, *Chem. Soc. Rev.*, 2020, **49**, 8–12.

13 Y. Deng, C. H. van Brackle, X. Dai, J. Zhao, B. Chen and J. Huang, *Sci. Adv.*, 2019, **5**, eaax7537.

14 X. Zheng, B. Chen, C. Wu and S. Priya, *Nano Energy*, 2015, **17**, 269–278.

15 T. Jeon, H. M. Jin, S. H. Lee, J. M. Lee, H. Il Park, M. K. Kim, K. J. Lee, B. Shin and S. O. Kim, *ACS Nano*, 2016, **10**, 7907–7914.

16 J. Niu, D. Yang, Z. Yang, D. Wang, X. Zhu, X. Zhang, S. Zuo, J. Feng and S. F. Liu, *ACS Appl. Mater. Interfaces*, 2018, **10**, 14744–14750.

17 D. K. Lee, D. N. Jeong, T. K. Ahn and N. G. Park, *ACS Energy Lett.*, 2019, **4**, 2393–2401.

18 K. H. Hendriks, J. J. Van Franeker, B. J. Bruijnaers, J. A. Anta, M. M. Wienk and R. A. J. Janssen, *J. Mater. Chem. A*, 2017, **5**, 2346–2354.

19 K. Wang, C. Wu, Y. Hou, D. Yang, W. Li, G. Deng, Y. Jiang and S. Priya, *Joule*, 2020, **4**, 615–630.

20 J. Málek and T. Mitsuhashi, *J. Am. Ceram. Soc.*, 2004, **83**, 2103–2105.

21 S. Baranovskii and O. Rubel, in *Springer Handbooks*, Springer, 2017, p. 1.

22 T. S. Sherkar, C. Momblona, L. Gil-Escrig, J. Ávila, M. Sessolo, H. J. Bolink and L. J. A. Koster, *ACS Energy Lett.*, 2017, **2**, 1214–1222.

23 R. A. Serway, C. J. Moses and C. A. Moyer, *Modern physics*, Thomson Brooks/Cole, 2005.

24 Z. Zhou, Z. Wang, Y. Zhou, S. Pang, D. Wang, H. Xu, Z. Liu, N. P. Padture and G. Cui, *Angew. Chemie Int. Ed.*, 2015, **54**, 9705–9709.

25 Z. Shao, Z. Wang, Z. Li, Y. Fan, H. Meng, R. Liu, Y. Wang, A. Hagfeldt, G. Cui and S. Pang, *Angew. Chemie Int. Ed.*, 2019, **58**, 5587–5591.

26 W. J. Yin, J. H. Yang, J. Kang, Y. Yan and S. H. Wei, *J. Mater. Chem. A*, 2015, **3**, 8926–8942.

27 F. K. Lotgering, *J. Inorg. Nucl. Chem.*, 1959, **9**, 113–123.

28 D. Shi, V. Adinolfi, R. Comin, M. Yuan, E. Alarousu, A. Buin, Y. Chen, S. Hoogland, A. Rothenberger, K. Katsiev, Y. Losovyj, X. Zhang, P. A. Dowben, O. F. Mohammed, E. H. Sargent and O. M. Bakr, *Science* 2015, **347**, 519–522.

29 S. Colella, E. Mosconi, P. Fedeli, A. Listorti, F. Gazza, F. Orlandi, P. Ferro, T. Besagni, A. Rizzo, G. Calestani, G. Gigli, F. De Angelis and R. Mosca, *Chem. Mater.*, 2013, **25**, 4613–4618.

30 N. Tripathi, M. Yanagida, Y. Shirai, T. Masuda, L. Han and K. Miyano, *J. Mater. Chem. A*, 2015, **3**, 12081–12088.

31 G. Xing, N. Mathews, S. Sun, S. S. Lim, Y. M. Lam, M. Graẗzel, S. Mhaisalkar and T. C. Sum, *Science* 2013, **342**, 344–347.

32 Y. Bai, X. Meng and S. Yang, *Adv. Energy Mater.*, 2018, **8**, 1701883.

33 J. K. J. van Duren, X. Yang, J. Loos, C. W. T. Bulle-Lieuwma, A. B. Sieval, J. C. Hummelen and R. A. J. Janssen, *Adv. Funct. Mater.*, 2004, **14**, 425–434.

34 S. S. Lim, W. K. Chong, A. Solanki, H. A. Dewi, S. Mhaisalkar, N. Mathews and T. C. Sum, *Phys. Chem. Chem. Phys.*, 2016, **18**, 27119–27123.

35 S. D. Stranks, G. E. Eperon, G. Grancini, C. Menelaou, M. J. P. Alcocer, T. Leijtens, L. M. Herz, A. Petrozza and H. J. Snaith, *Science* 2013, **342**, 341–344.

36 G. Schuck, F. Lehmann, J. Ollivier, H. Mutka and S. Schorr, *J. Phys. Chem. C*, 2019, **123**, 11436–11446.

37 E. L. Unger, A. R. Bowring, C. J. Tassone, V. L. Pool, A. Gold-Parker, R. Cheacharoen,

K. H. Stone, E. T. Hoke, M. F. Toney and M. D. McGehee, *Chem. Mater.*, 2014, **26**, 7158–7165.

38 F. Zhang, B. Yang, Y. Li, W. Deng and R. He, *J. Mater. Chem. C*, 2017, **5**, 8431–8435.

39 A. Klasen, P. Baumli, Q. Sheng, E. Johannes, S. A. Bretschneider, I. M. Hermes, V. W. Bergmann, C. Gort, A. Axt, S. A. L. Weber, H. Kim, H. J. Butt, W. Tremel and R. Berger, *J. Phys. Chem. C*, 2019, **123**, 13458–13466.

40 C. M. Yim, C. L. Pang and G. Thornton, *Phys. Rev. Lett.*, 2010, **104**, 036806.

41 Y. Cheng, F. So and S. W. Tsang, *Mater. Horizons*, 2019, 6, 1611–1624.

42 T.-C. Sum and N. Mathews, *Halide Perovskites : Photovoltaics, light emitting devices and beyond*, Wiley-VCH, 2018.

43 M. I. Saidaminov, A. L. Abdelhady, B. Murali, E. Alarousu, V. M. Burlakov, W. Peng, I. Dursun, L. Wang, Y. He, G. MacUlan, A. Goriely, T. Wu, O. F. Mohammed and O. M. Bakr, *Nat. Commun.*, 2015, **6**, 1–6.

44 Tingyu Song, Lifeng Gao, L. Y. Qi Wei, Shiwei Wang, Mingyao Zhang, Lisha Zhao and Yanhua Cai, *Mater. Res. Express*, 2020, **7**, 015522.

45 Z. Liu, J. Chang, Z. Lin, L. Zhou, Z. Yang, D. Chen, C. Zhang, S. F. Liu and Y. Hao, *Adv. Energy Mater.*, 2018, **8**, 1703432.

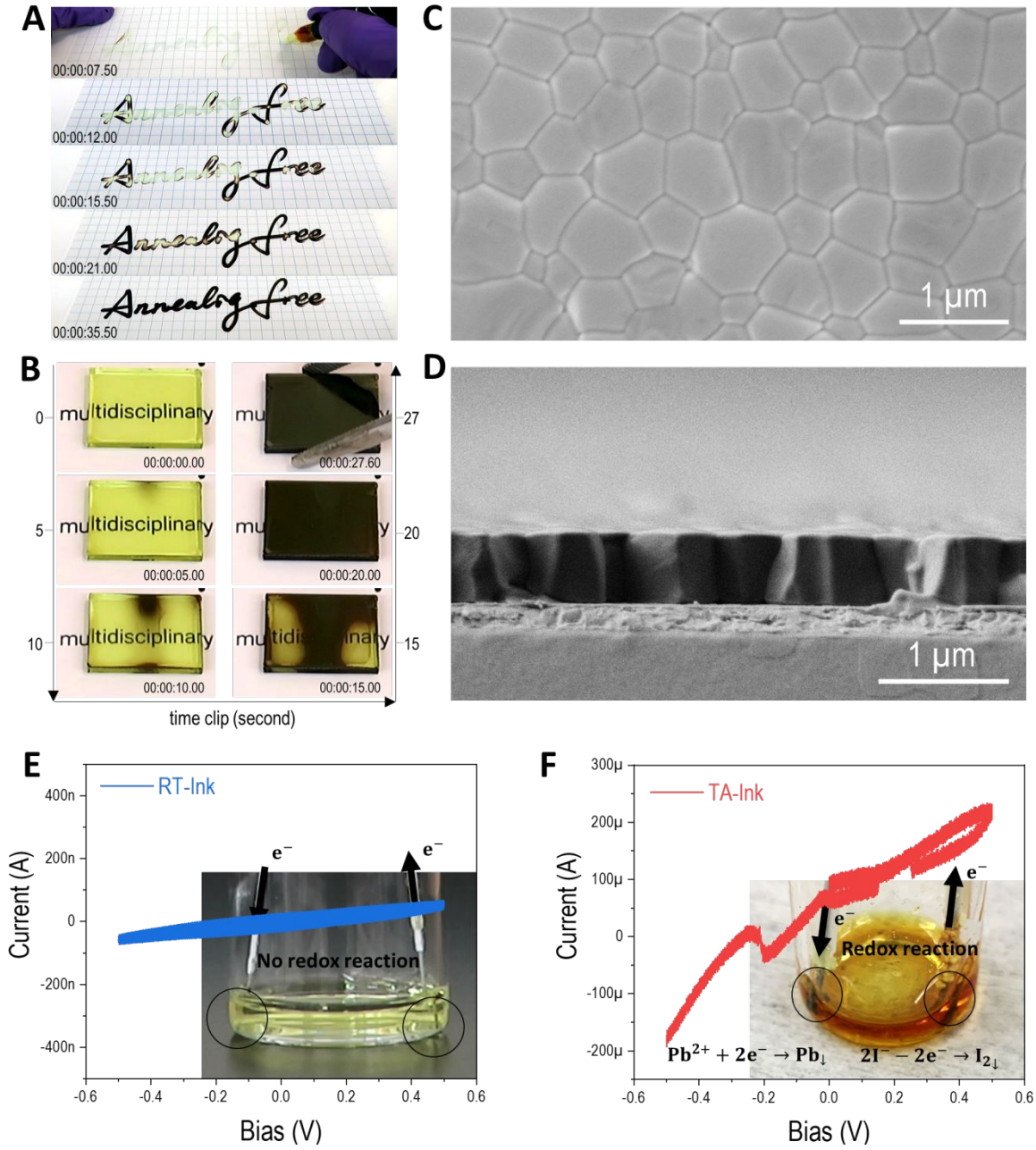

Fig. 1 Writing with RT rapidly crystallized perovskite ink. Snapshots showing the rapid RT-isothermal crystallization **(A)** during handwriting on a paper and **(B)** in a blade-coated film. Microscopic feature of the RT isothermally crystallized film in a **(C)** top-view and **(D)** cross-sectional view acquired from scanning electron microscopy. **(E, F)** Verification of minimized free ions in RT-ink: **(E)** a RT-ink: ionic current vs. bias plot (measured by a cyclic voltammetry measurement using the ink as electrolyte), the insert picture shows a RT-ink under bias of 1.5 V after aging for 5 hr., exhibiting no precipitation; **(F)** a typical TA-ink: ionic current vs. bias, the current at 0.4 V exhibits a number over 200 μA, a picture shows a TA-ink under bias of 1.5 V after aging for 5 hr., where the I_2 and Pb precipitations suggest the proceeding of the redox reaction.

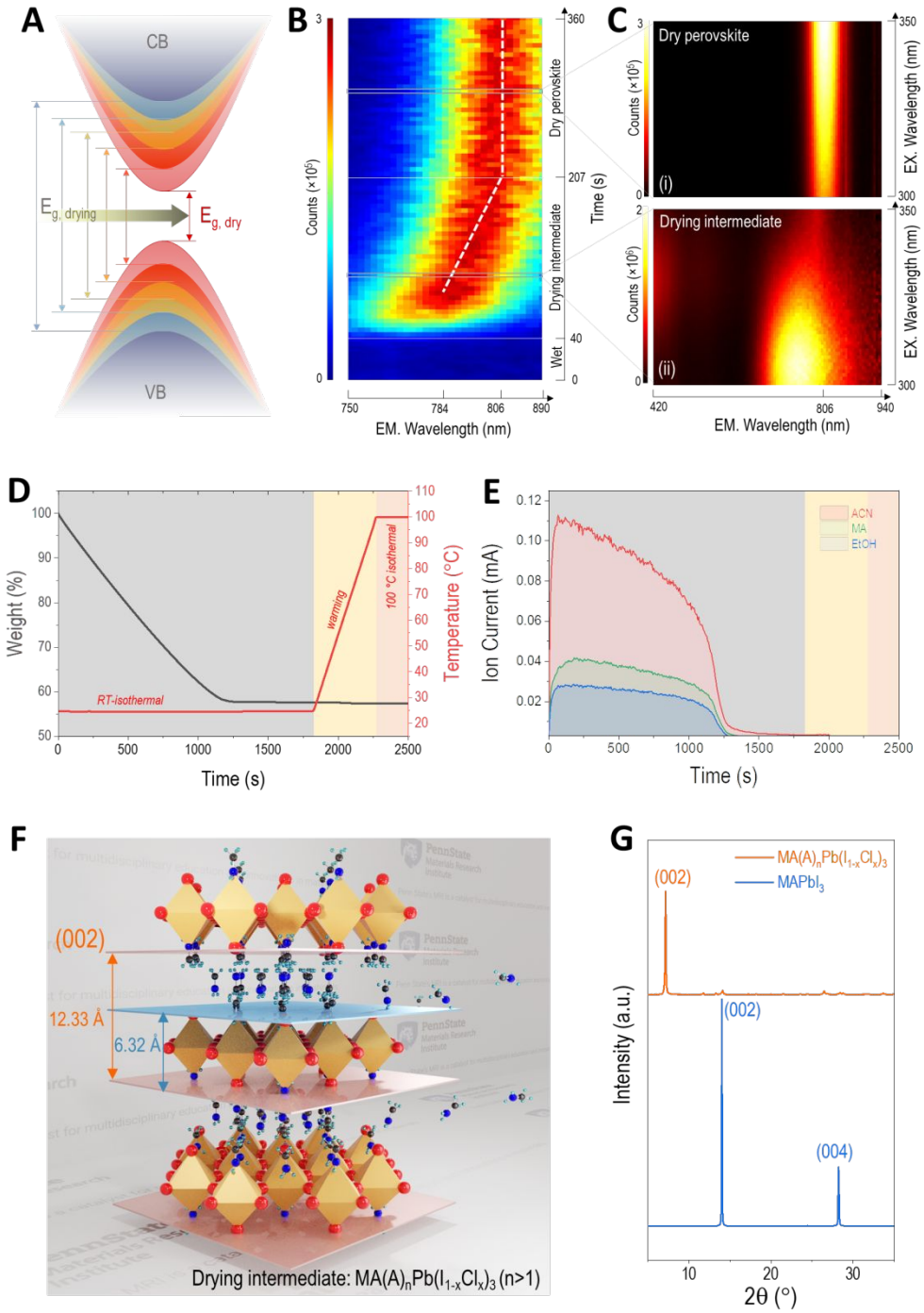

Fig. 2 Compositional evolution during RT isothermal crystallization. (A) Illustrative band-gap reduction and **(B)** corresponding experimental photoluminescence (PL) change upon time-development during film drying process. **(C)** Time-integrated PL-map comparison between dried crystal and drying intermediate. **(D)** Thermogravimetric analysis (TGA) of RT isothermal crystallization ink coupled with **(E)** an *in-situ* mass spectroscopy (MS) investigation. **(F)** Schematic illustration of the amine escaping from the lattice of intermediate perovskite during the drying and **(G)** an XRD comparison between final crystal and intermediate perovskite.

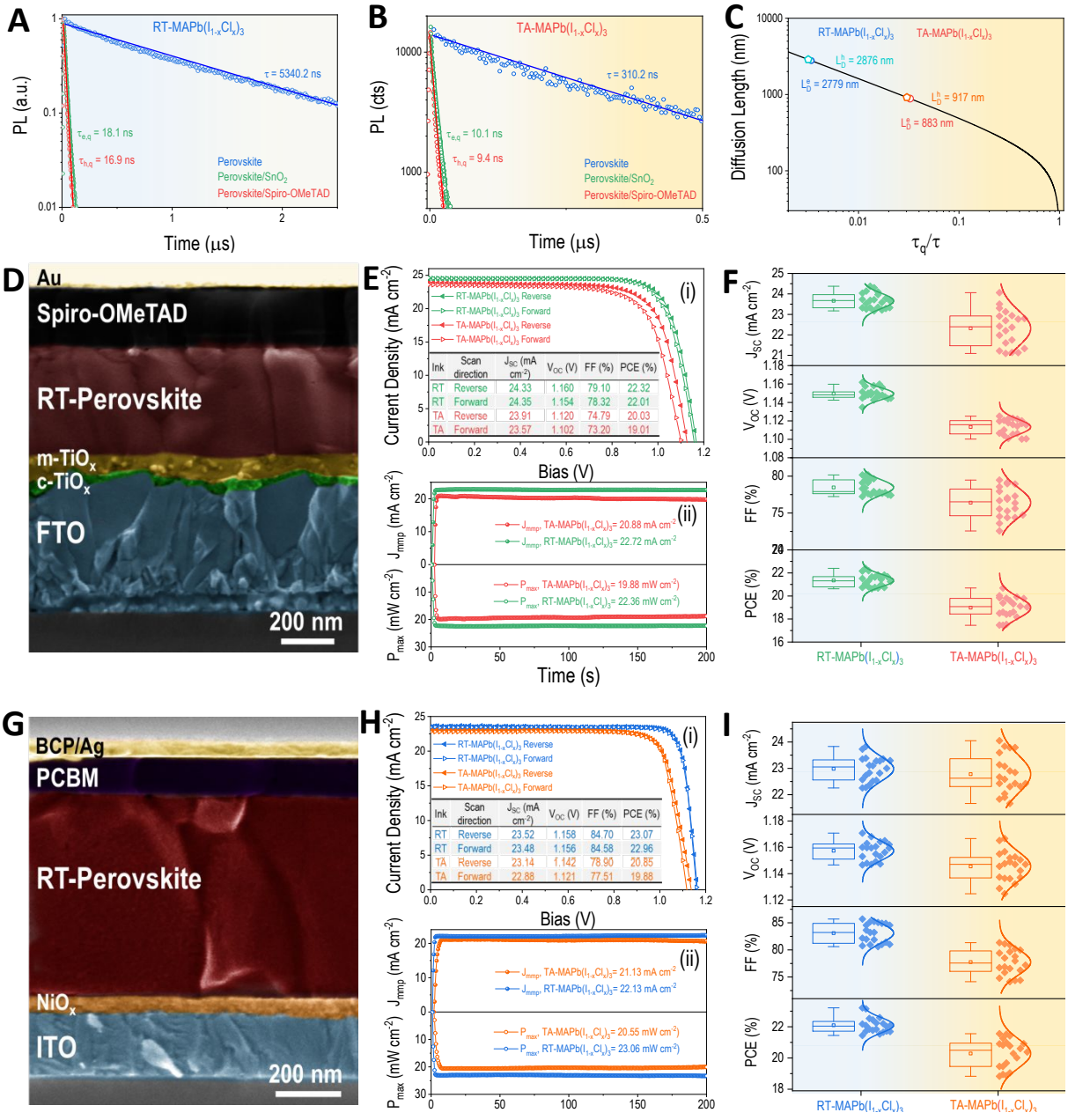

Fig. 3 Long carrier diffusion length in RT-perovskite film and their PV device performance. Diffusion model analysis for charge carrier diffusion length (A-C): time-resolved PL decay transients for perovskite without the quencher layer (blue), with the electron quencher layer (green), and with the hole quencher layer (red), where the perovskite is **(A)** RT-perovskite and **(B)** TA-perovskite, respectively. **(C)** Exciton diffusion length versus PL lifetime quenching ratios on the basis of **Equation 1** (specified in the **Supplemental Note S4**). **Conventional device performance (D-F): (D)** cross-sectional SEM image of the whole n-i-p device using RT-perovskite; **(E)** (i) J-V characteristics and (ii) static current density at maximal output power point and corresponding PCE measured as a function of time for both RT-perovskite and TA-perovskite based n-i-p device; **(F)** Statistics of photovoltaic parameters of perovskite solar cells using RT-perovskite and TA-

perovskite. **Inverted device performance (G-I): (G)** cross-sectional SEM image of the whole p-i-n device using RT-perovskite; **(H)** (i) J-V characteristics and (ii) static current density at maximal output power point and corresponding PCE measured as a function of time for both RT-perovskite and TA-perovskite based p-i-n device; **(I)** Statistics of photovoltaic parameters of perovskite solar cells using RT-perovskite and TA-perovskite.